



# Constructing the Fe/Cr double (oxy)hydroxides on Fe<sub>3</sub>O<sub>4</sub> for boosting the electrochemical oxygen evolution in alkaline seawater and domestic sewage

Lu Li<sup>a,1</sup>, Gengwei Zhang<sup>a,1</sup>, Bin Wang<sup>a,b,\*</sup>, Shengchun Yang<sup>a,b</sup>

<sup>a</sup> School of Physics, MOE Key Laboratory for Non-equilibrium Synthesis and Modulation of Condensed Matter, Key Laboratory of Shaanxi for Advanced Materials and Mesoscopic Physics, State Key Laboratory for Mechanical Behavior of Materials, Xi'an Jiaotong University, Xi'an 710049, People's Republic of China

<sup>b</sup> Shaanxi Collaborative Innovation Center for Hydrogen Fuel Cell Performance Improvement, Xi'an Jiaotong University, People's Republic of China

## ARTICLE INFO

### Keywords:

Oxygen evolution reaction  
Metal oxyhydroxide  
Mass production  
Interface engineering

## ABSTRACT

Developing the electrocatalysts which can be directly performed in sewage and seawater without further treatment kills two birds with one stone since it can turn waste into raw materials and produce H<sub>2</sub>. Herein, the heterointerface between Fe(Cr)OOH and Fe<sub>3</sub>O<sub>4</sub> is constructed through a scalable method. Systematic experiments and theoretical calculations confirmed that the Fe(Cr)OOH coupling with Fe<sub>3</sub>O<sub>4</sub> can significantly decrease the oxygen evolution reaction (OER) overpotential ( $\eta_{500} = 241$  mV in 1 M KOH) and promote the mass and electron transfer. Impressively, this electrode could work efficiently and maintain 100 mA cm<sup>-2</sup> for 100 h in both alkaline seawater and domestic sewage. The electrolyzer using such electrode as anode could deliver a current density of 500 mA cm<sup>-2</sup> in 5 M KOH at a small cell voltage of 1.62 V. This work provides a facile route to prepare efficient and low-cost OER catalysts, which has important implications for energy conversion.

## 1. Introduction

Hydrogen has been considered as a promising energy carrier due to its characteristics of high energy density and zero CO<sub>2</sub> emission [1]. As an ideal approach to produce hydrogen, water electrolysis could transform excess energy from renewable sources into hydrogen, which has drawn tremendous attention in recent years [2–14]. It has been considered that water electrolysis in alkaline solution is more attractive than that in acidic conditions, which are mainly due to the insufficient stability of electrocatalyst for oxygen evolution reaction (OER) in acidic electrolytes [15,16]. Up to now, 95% of hydrogen is still produced by steam reforming which generates large amounts of CO<sub>2</sub> byproduct, while less than 4% hydrogen is produced by electrolysis [17,18]. Currently, the cost of water electrolysis is around 4 dollars per kilogram of H<sub>2</sub>, which is more expensive than that of fossil-fuels reforming (around 1.3 dollars per kilogram of H<sub>2</sub>) [19], thus impeding the spread and application of water electrolysis. The four-electron-transfer OER process with sluggish kinetics has been considered as the main

bottleneck in water electrolysis, resulting in a large energy barrier [20]. Thus, it is urgent to develop highly active catalysts that can decrease energy consumption during the OER process [21]. Although great progress has been made to develop OER electrocatalysts in the lab [15, 18,20,22], most of them are far from the high criteria for practical applications. It is required that the electrode can be facilely produced on a large scale, and capable to work efficiently and steadily at high output [23,24]. Specifically, the alkaline electrolyzer should deliver a rather large current density of 500 mA cm<sup>-2</sup> with an overpotential lower than 300 mV for a long period [25,26]. These gaps restrict the abroad application of the water-splitting catalysts. In addition, many catalysts are in powder forms, which are easy to peel off from the current collector during the electrolysis, especially with intensively evolved bubbles at high output [27,28]. Fabricating the active material directly on the substrate could effectively enhance the mechanical stability and electronic conductivity of the electrode, thus improving its catalytic performance. However, traditional synthesis approaches of the self-supported electrode, including hydrothermal method,

\* Corresponding author at: School of Physics, MOE Key Laboratory for Non-equilibrium Synthesis and Modulation of Condensed Matter, Key Laboratory of Shaanxi for Advanced Materials and Mesoscopic Physics, State Key Laboratory for Mechanical Behavior of Materials, Xi'an Jiaotong University, Xi'an 710049, People's Republic of China.

E-mail addresses: [bin\\_wang@xjtu.edu.cn](mailto:bin_wang@xjtu.edu.cn) (B. Wang), [ysch1209@mail.xjtu.edu.cn](mailto:ysch1209@mail.xjtu.edu.cn) (S. Yang).

<sup>1</sup> Gengwei Zhang and Lu Li contribute equally to this work.

electro-deposition and chemical vapor deposition, have many disadvantages such as high-cost and complex technics flow, and even with noxious reagents [29]. Moreover, it is difficult to precisely control the synthesis condition in a scale-up production process, which could lead to large discrepancies of the produced electrode. These disadvantages limit the practical application of the catalyst from lab to industrial scale. Therefore, it is still challenging to develop an easy scale-up method to prepare OER electrocatalysts with high activity and durability at large current densities for water electrolysis.

FeOOH is a promising candidate electrocatalyst material for OER due to its low cost, high activity and stability [30,31]. However, the poor electrical conductivity of metal oxyhydroxide greatly limits its catalytic performance [30–34]. Besides, the  $\text{OH}_{\text{ad}}$  adsorption of FeOOH is too strong and accordingly its performance has the potential to be further improved [30,32]. Therefore, developing a durable efficient OER catalyst based on FeOOH is of significant practical value and highly desirable. Surface modification could offer hydrophilicity to promote the gas release and mass exchange, which is critical for electrocatalytic water splitting at high current densities [33]. Constructing heterostructure with abundant interfaces could tailor the electronic property of the catalyst and thus achieve a high intrinsic activity and electronic conductivity [34–37]. For instance, Li et al. synthesized the heterostructured  $\text{NiCo}_2\text{S}_4/\text{FeOOH}$  nanowire with a remarkable activity for OER [38]. Recently, it was reported that the oxophilic first-row transition element, such as Ti, Co and Cr, could modulate the binding energy of oxygen-containing intermediate [39,40]. And the special electronic configuration of Cr cation could improve the electrochemical process in terms of charge transfer [41]. Therefore, it is reasonable to speculate that the incorporation of Cr into FeOOH could boost the OER performance.

Another consideration is that, the electrolyte prepared with ultrapure water is generally used for water electrolysis in the lab, which is uneconomical for hydrogen production on an industrial scale. Seawater, which constitutes 97% of the water resource in nature [42], along with domestic sewage, can be ideal alternatives to prepare electrolytes for large-scale water electrolysis. Moreover, an alkaline electrolyte is more appropriate for seawater electrolysis to avoid generating hypochlorite [43]. Nevertheless, some challenges still stay in the way of hydrogen production from seawater or sewage. The complex composition and chloride corrosion from such water sources might degrade the catalytic efficiency of the electrocatalyst. What's more, a high concentration aqueous KOH solution (25–30 wt%) is generally used as the electrolyte in industrial alkaline water electrolyzer [44,45]. Hence, it is essential to develop electrocatalysts with retention of activity and stability under such harsh conditions.

With this in mind, herein we constructed the heterointerface between  $\text{Fe}(\text{Cr})\text{OOH}$  and  $\text{Fe}_3\text{O}_4$  on Ni foam via a simple and scalable approach. The as-prepared  $\text{Fe}(\text{Cr})\text{OOH}/\text{Fe}_3\text{O}_4/\text{NF}$  with a hydrophilic surface can achieve a high anodic current density of  $500 \text{ mA cm}^{-2}$  with a small overpotential of 241 mV. Theoretical calculations reveal that the introduction of Cr and the coupling with  $\text{Fe}_3\text{O}_4$  could drastically lower the energy barrier for OER, and increase the electrical conductivity of the catalyst. The electrolyzer using such electrode as anode reaches the current densities of 10 and  $500 \text{ mA cm}^{-2}$  with small cell voltages of 1.46 and 1.62 V for overall water splitting in 5 M KOH, respectively. This electrolyzer could also work efficiently in both alkaline domestic sewage and seawater, and maintain a  $400 \text{ mA cm}^{-2}$  current density for 100 h. This work affords a facile method to prepare highly efficient and cost-effective OER electrocatalysts, which could offer references to the catalyst design for practical water electrolysis.

## 2. Experimental section

### 2.1. Preparation of $\text{Fe}_3\text{O}_4/\text{NF}$

Firstly, commercial Ni foam was ultrasonically cleaned with 3 M HCl,

ethanol, and ultrapure water. An ink was prepared by dissolving 6.5 g  $\text{Fe}(\text{NO}_3)_3 \cdot 9\text{H}_2\text{O}$  and 0.8 g polyvinylpyrrolidone (PVP) in 35 mL N, N-dimethylformamide (DMF) and stirred for 30 min at  $70^\circ\text{C}$ . Afterwards, NF was directly immersed in the ink and then dried in the air. Finally, the dried NF was annealed in air at  $350^\circ\text{C}$  for 1 h with a heating rate of  $5^\circ\text{C min}^{-1}$ . The product was labeled as  $\text{Fe}_3\text{O}_4/\text{NF}$ .

### 2.2. Preparation of $\text{Fe}(\text{Cr})\text{OOH}/\text{Fe}_3\text{O}_4/\text{NF}$

The formation of  $\text{Fe}(\text{Cr})\text{OOH}$  on  $\text{Fe}_3\text{O}_4/\text{NF}$  was achieved by a facile impregnation method. Firstly, the reaction solution was prepared by dissolving 0.96 g  $\text{FeCl}_3 \cdot 6\text{H}_2\text{O}$ , 0.95 g  $\text{Cr}(\text{NO}_3)_3 \cdot 9\text{H}_2\text{O}$  and 3.4 g  $\text{NaNO}_3$  into 40 mL water, the atomic fraction of  $\text{Cr}^{3+}/(\text{Fe}^{3+} + \text{Cr}^{3+})$  is 0.4, the solution was stirred and heated to  $80^\circ\text{C}$  for 20 min. Next, the  $\text{Fe}_3\text{O}_4/\text{NF}$  was immersed in the above-preheated solution for 5 min. After that, the prepared samples were washed with water and then dried. The obtained product was named  $\text{Fe}(\text{Cr})\text{OOH}/\text{Fe}_3\text{O}_4/\text{NF}$ . The mass loading of  $\text{Fe}(\text{Cr})\text{OOH}/\text{Fe}_3\text{O}_4$  on NF was about  $2.6 \text{ mg cm}^{-2}$ . For contrast,  $\text{Fe}(\text{Cr})\text{OOH}/\text{Fe}_3\text{O}_4/\text{NF}$  samples were prepared with impregnation solutions of various molar ratios ( $\text{Cr}^{3+}/[\text{Fe}^{3+} + \text{Cr}^{3+}] = 0, 0.2, 0.6, 0.8$ ).  $\text{Fe}(\text{Cr})\text{OOH}/\text{NF}$  ( $\text{Cr}^{3+}/[\text{Fe}^{3+} + \text{Cr}^{3+}] = 0.4$ ) and  $\text{FeOOH}/\text{NF}$  were also prepared via the same method by using blank NF instead of  $\text{Fe}_3\text{O}_4/\text{NF}$ .

### 2.3. Electrochemical measurements

All electrochemical investigations were performed at room temperature on a CHI 760E electrochemical workstation (CHI Instruments, Shanghai Chenhua Instrument Corporation, China) using a carbon rod as the counter electrode, and a Hg/HgO electrode as the reference electrode. The prepared samples were used as the working electrodes and measured in different electrolytes, including 1 M KOH, 5 M KOH, 1 M KOH + sewage and 1 M KOH + seawater. All the potentials reported in this work were referenced to reversible hydrogen electrode (RHE). The reference electrode was calibrated experimentally at the end of electrochemical studies, using a Pt wire in the electrolyte saturated with  $\text{H}_2$ . All the linear sweep voltammetry (LSV) curves were reported with  $iR$  correction and the scan rate is  $1 \text{ mV s}^{-1}$  to minimize the effect of the capacitive current. To avoid interference due to the pre-OER oxidation, the curves were recorded from high to low potentials. Electrochemical impedance spectroscopy (EIS) was performed under a fixed bias of 100 mV with the frequency range from 100 kHz to 0.1 Hz. Double-layer capacitance ( $C_{\text{dl}}$ ) data were collected by measuring the cyclic voltammetry (CV) curves with various scan rates (2, 4, 6, 8 and  $10 \text{ mV s}^{-1}$ ). For faradaic efficiency (FE) determination, the theoretical amount of  $\text{O}_2$  was calculated based on the Faraday law, the actual generated  $\text{O}_2$  amount was tested via a Hoffman apparatus setup in a two-electrode system. Constant-current electrolysis was carried out and the volume of oxygen was recorded every 10 min.

### 2.4. Model and computation detail

The calculations were carried out with the density functional theory (DFT) as implemented in the Vienna ab initio simulation package (VASP). The exchange-correlation functional was described within the generalized gradient approximation (GGA) parameterized by the Perdew-Burke-Ernzerhof (PBE). The vdW correction was considered by employing the Grimme's D3. The cut-off energy for the plane-wave basis was set to 400 eV. To better describe Coulomb interaction in the localized 3d orbitals and magnetic interaction, an effective U of 4 eV for Fe d-states and an effective U of 6 eV for Cr d-states were used in this study [46]. A vacuum region of  $15 \text{ \AA}$  perpendicular to the surface was applied to avoid interaction between neighboring surfaces. Atoms were relaxed until the Hellmann-Feynman forces acting on them were less than  $0.02 \text{ eV/\AA}$ .  $\text{Fe}_3\text{O}_4$  was modeled as a  $(2 \times 1)$  surface unit cell of four-layered  $\text{Fe}_3\text{O}_4$  (111). FeOOH was modeled as a  $(2 \times 1)$  surface unit cell of four-layered FeOOH (100). To simulate the  $\text{FeOOH}/\text{Fe}_3\text{O}_4$  interface, The

FeOOH was deposited on a four-layer Fe<sub>3</sub>O<sub>4</sub> (111) slab. The Brillouin zone was sampled by a (3 × 3 × 1) Gamma-centered k-mesh. The adsorption free energy for adsorbates ( $\Delta G_{ads}$ ) in OER can be calculated by the following equation:

$$\Delta G_{ads} = \Delta E_{ads} + \Delta E_{ZPE} - T\Delta S \quad (1)$$

where  $\Delta E_{ads}$  is the adsorption energy of adsorbates, and  $T$  is temperature.  $\Delta E_{ZPE}$  and  $\Delta S$  are the energy difference in zero-point energy and entropy, respectively, which were obtained based on vibration analysis. OER activity is evaluated by the following four elementary steps.



The adsorption energy of intermediates (O\*, OH\*, OOH\*) on (\*) substrate were determined by the following approach of Nørskov et al. [47]

$$\Delta E_{O*} = E_{OH*} - E_{(*)} - (E_{H_2O} - 1/2E_{H_2}) \quad (6)$$

$$\Delta E_{OH*} = E_{O*} - \Delta E_{(*)} - (E_{H_2O} - E_{H_2}) \quad (7)$$

$$\Delta E_{OOH*} = E_{OOH*} - \Delta E_{(*)} - (2E_{H_2O} - 3/2E_{H_2}) \quad (8)$$

Where  $E_{(*)}$ ,  $E_{HO*}$ ,  $E_{O*}$ , and  $E_{HOO*}$  are the total energies of the pure surface and the adsorbed surface with HO\*, O\*, and HOO\*, respectively,  $E_{H_2O}$  is the computed energy for the sole H<sub>2</sub>O molecule. The Gibbs free energy changes for steps 2–5 can be expressed as follows:

$$\Delta G_1 = \Delta G_{OH*} - eU \quad (9)$$

$$\Delta G_2 = \Delta G_{O*} - \Delta G_{OH*} - eU \quad (10)$$

$$\Delta G_3 = \Delta G_{OOH*} - \Delta G_{O*} - eU \quad (11)$$

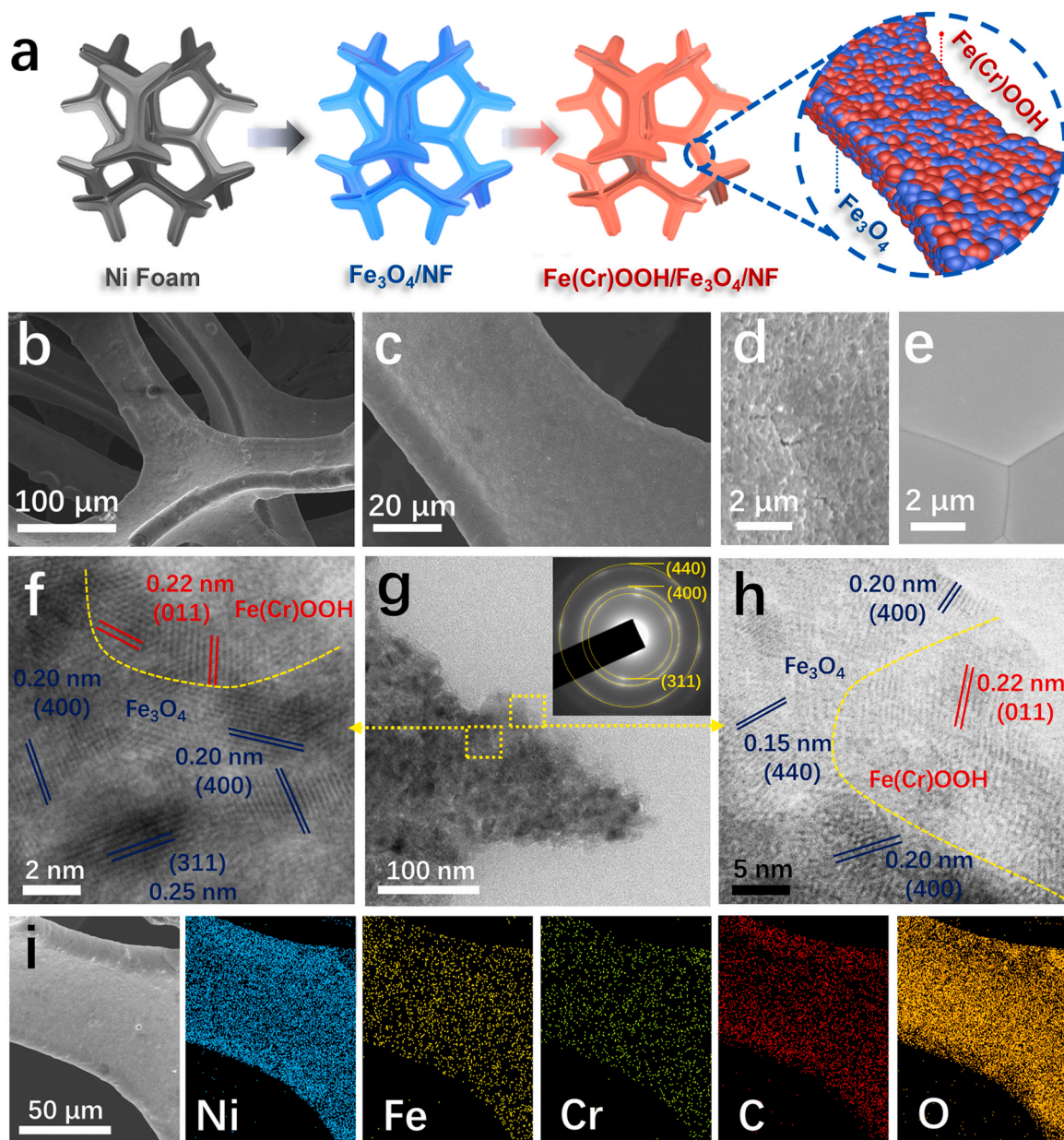


**Fig. 1.** (a) Schematic of the preparation of the Fe(Cr)OOH/Fe<sub>3</sub>O<sub>4</sub>/NF. (b–d) SEM images of Fe(Cr)OOH/Fe<sub>3</sub>O<sub>4</sub>/NF and (e) blank NF at different magnifications. (g) TEM image, SAED pattern, (f, h) HRTEM images of Fe(Cr)OOH/Fe<sub>3</sub>O<sub>4</sub>/NF. (i) EDX mapping images of Fe(Cr)OOH/Fe<sub>3</sub>O<sub>4</sub>/NF.



$$\Delta G_4 = 4.92 - \Delta G_{OOH^*} - eU \quad (12)$$

Where  $U$  is the applied voltage. The theoretical overpotentials ( $\eta$ ) for OER can be calculated by the following equations:

$$G_{OER} = \max \{ \Delta G_1, \Delta G_2, \Delta G_3, \Delta G_4 \} \quad (13)$$

$$\eta = G_{OER}/e - 1.23 \text{ V} \quad (14)$$

### 3. Results and discussion

#### 3.1. Morphological and structural analysis

The Fe(Cr)OOH/Fe<sub>3</sub>O<sub>4</sub> hybrid catalyst was fabricated via a facile impregnation method (Fig. 1a). Firstly, the bare Ni foam was immersed into Fe<sup>3+</sup> solution, followed by annealing to fabricate Fe<sub>3</sub>O<sub>4</sub>/NF, and then it was immersed in a solution containing both Fe<sup>3+</sup> and Cr<sup>3+</sup> at 80 °C to fabricate Fe(Cr)OOH/Fe<sub>3</sub>O<sub>4</sub>/NF. After the preparation, the morphology of the sample was investigated by scanning electron microscope (SEM). Fig. S1 shows a 3D porous skeleton structure of the blank Ni foam. The Fe<sub>3</sub>O<sub>4</sub>/NF retains the skeleton structure while the surface becomes rough and porous (Fig. S2 and S3). As shown in Fig. 1b–d, the subsequent Fe(Cr)OOH/Fe<sub>3</sub>O<sub>4</sub> sample maintains a more rough surface compared with that of the Ni foam (Fig. 1e), which could provide more active sites, meanwhile, improve the surface hydrophilicity [48,49]. Such surface structure has been widely recognized as helpful

for the OER process [33]. Transmission electron microscope (TEM) was performed to further reveal the microstructure of Fe(Cr)OOH/Fe<sub>3</sub>O<sub>4</sub> layer. Fig. 1g demonstrated that the Fe(Cr)OOH/Fe<sub>3</sub>O<sub>4</sub> layer consists of a large number of nanoparticles. The selected area electron diffraction (SAED) pattern displays the diffraction rings corresponding to the (440), (400) and (311) planes of Fe<sub>3</sub>O<sub>4</sub>, confirming that Fe<sub>3</sub>O<sub>4</sub> was successfully formed by annealing, and retained after the impregnation. No characteristic electron diffractions could be indexed to FeOOH, which may be due to the low crystallinity of oxyhydroxide. High-resolution TEM (HRTEM) images (Fig. 1f and h) show the short-range lattice fringes of Fe(Cr)OOH/Fe<sub>3</sub>O<sub>4</sub>, suggesting the low crystallinity. The spacings of 0.15, 0.20 and 0.25 nm agree with the distance of (440), (400) and (311) planes of Fe<sub>3</sub>O<sub>4</sub>, respectively [38], and the lattice fringe spacing of 0.22 nm matches with the (011) plane of FeOOH [50]. The Energy Dispersive X-ray (EDX) mapping in Fig. 1i confirm the existence and homogeneous distribution of elemental Fe, Cr, O and C. The nickel and carbon signals come from the Ni foam and residual PVP, respectively.

The X-ray diffraction (XRD) and Raman spectroscopy were conducted to determine the structure of the catalysts. The XRD pattern in Fig. 2a shows a set of diffraction peaks at 30.1°, 35.4°, 43.1°, 56.9° and 62.5° from Cubic Fe<sub>3</sub>O<sub>4</sub> phase (JCPDS No. 65-3107), and the peaks at 44.5°, 51.8°, and 76.4° come from Ni foam (JCPDS No. 01-1258), further confirming the formation of Fe<sub>3</sub>O<sub>4</sub> on NF. After modified by impregnation solution, no new crystallization peak appears due to the low crystallinity of the oxyhydroxide. While the Raman spectrum in Fig. 2b confirms the formation of FeOOH with typical peaks at 250, 310, 379, 413, 486, 540 and 680 cm<sup>-1</sup> [30,36]. X-ray photoelectron

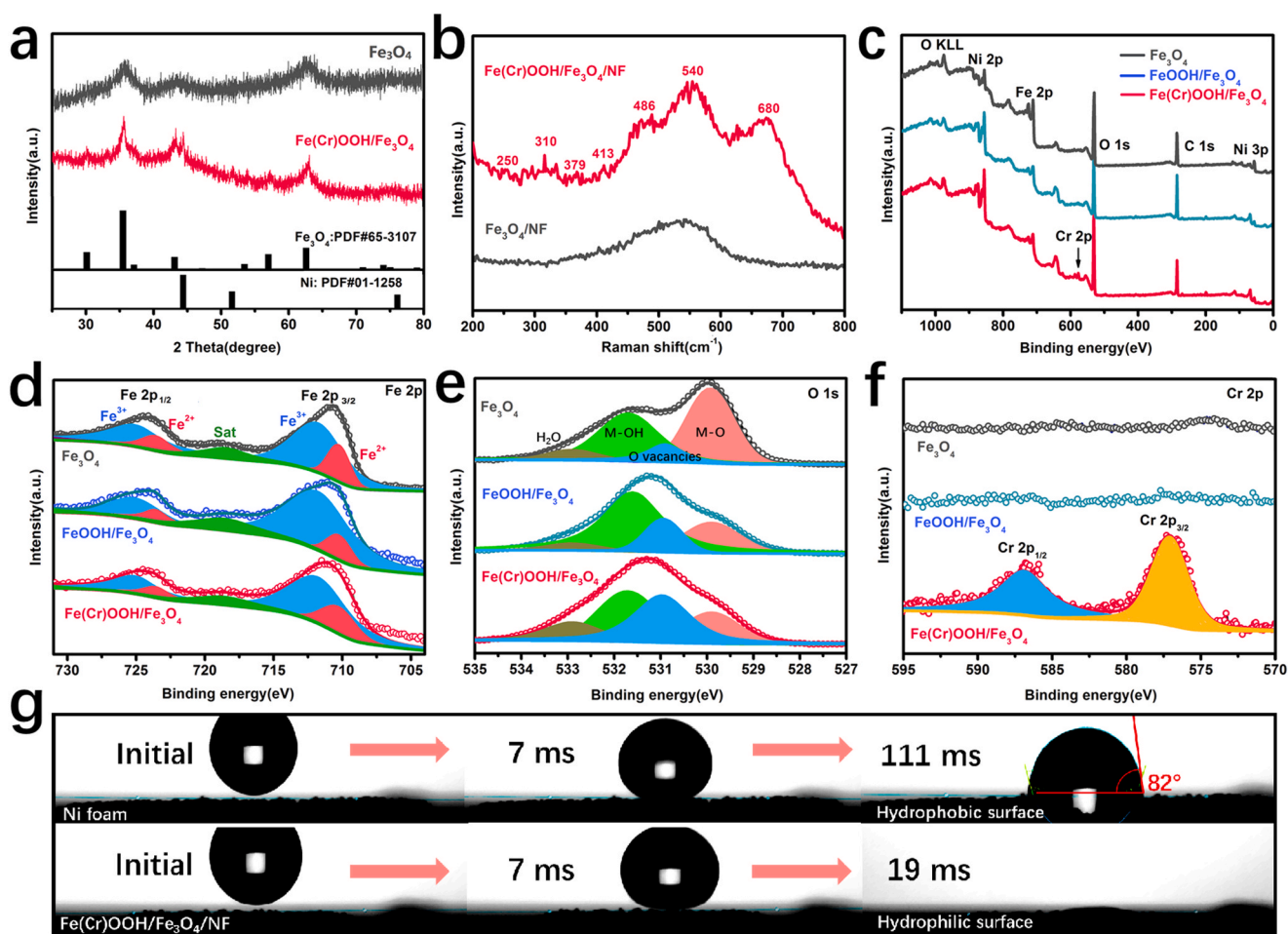


**Fig. 2.** (a) XRD patterns and (b) Raman spectra of Fe(Cr)OOH/Fe<sub>3</sub>O<sub>4</sub>/NF and Fe<sub>3</sub>O<sub>4</sub>/NF. XPS analysis of Fe<sub>3</sub>O<sub>4</sub>/NF, FeOOH/Fe<sub>3</sub>O<sub>4</sub>/NF and Fe(Cr)OOH/Fe<sub>3</sub>O<sub>4</sub>/NF. (c) Wide-scanning XPS spectra. High-resolution XPS spectra of (d) Fe 2p, (e) O 1s and (f) Cr 2p. (g) Photos of contact angle measurements of bare NF and Fe(Cr)OOH/Fe<sub>3</sub>O<sub>4</sub>/NF.



spectroscopy (XPS) was obtained to analyze the elemental chemical states of the samples. In the high-resolution Fe 2p spectrum of  $\text{Fe}_3\text{O}_4$  (Fig. 3d), two core-level signals located at 710.7 and 724.4 eV are assigned to Fe 2p<sub>3/2</sub> and 2p<sub>1/2</sub>, respectively. The deconvoluted peaks located at 712.1 and 725.3 eV are due to  $\text{Fe}^{3+}$ , the other two peaks situated at 710.4 and 723.5 eV are assigned to  $\text{Fe}^{2+}$ , and the satellite's peaks at 718.8 eV is also simulated out [51]. The atomic ratio of  $\text{Fe}^{2+}/\text{Fe}^{3+}$  is about 1:2, which is in accordance with the composition of  $\text{Fe}_3\text{O}_4$ . By contrast, the  $\text{FeOOH}/\text{Fe}_3\text{O}_4$  shows increased  $\text{Fe}^{3+}/\text{Fe}^{2+}$  ratios in both Fe 2p<sub>3/2</sub> and 2p<sub>1/2</sub> regions, which further indicates the presence of  $\text{FeOOH}$ . After incorporating with Cr, the ratio of  $\text{Fe}^{2+}$  shows an obvious increase which can be attributed to the larger electronegativity of Fe than that of Cr, leading to the electron transfer from Cr atoms to Fe atoms. In the O 1s core-level XPS spectrum of  $\text{Fe}_3\text{O}_4$ , the peaks situated at 529.9, 531.8, 530.9 and 532.9 eV could be attributed to lattice oxygen, hydroxyl oxygen, oxygen vacancy and adsorbed water, respectively [35,52]. The ratio of oxygen defect site increased after the coupling of  $\text{FeOOH}$  and  $\text{Fe}_3\text{O}_4$ , and further increased after incorporating with Cr. A new signal of Cr appeared in the spectra of  $\text{Fe}(\text{Cr})\text{OOH}/\text{Fe}_3\text{O}_4$  (Fig. 2c and f), demonstrating the existence of Cr. The Cr XPS spectrum exhibits two peaks at 587.2 (Cr 2p<sub>1/2</sub>) and 577.4 eV (Cr 2p<sub>3/2</sub>), which are in accordance with  $\text{Cr}^{3+}$  [53]. The wettability of the electrodes is characterized by contact angle measurements. Fig. 2g shows that the contact angle of 1 M KOH aqueous solution on NF is 82° (111 ms), indicating the poor water adhesion property of NF. In contrast, the liquid droplet

rapidly infiltrates into the  $\text{Fe}(\text{Cr})\text{OOH}/\text{Fe}_3\text{O}_4/\text{NF}$  electrode with no contact angle observed (19 ms), revealing a super-hydrophilicity of the electrode, which could improve the electrolyte penetration [54,55].

### 3.2. Electrochemical analysis

The electrocatalytic performance of the catalyst was tested in 1 M KOH. The cyclic voltammetry (CV) curves of the as-prepared catalysts in Fig. S4 exhibit the  $\text{Ni}^{2+}/\text{Ni}^{3+}$  redox peaks between 1.25 and 1.4 V prior to the OER. To avoid the signal overlap of the OER and  $\text{Ni}^{2+}/\text{Ni}^{3+}$  oxidation, the linear-sweep voltammetry (LSV) plots were recorded from high potential to low potential. The linear-sweep voltammetry (LSV) plots in Fig. 3a and b show that the bare NF exhibits a poor OER performance, and the  $\text{Fe}_3\text{O}_4/\text{NF}$  requires an overpotential of 267 mV to deliver a current density of  $10 \text{ mA cm}^{-2}$ , which is remarkably higher than that of  $\text{FeOOH}/\text{Fe}_3\text{O}_4/\text{NF}$  (213 mV). Furthermore, the  $\text{Fe}(\text{Cr})\text{OOH}/\text{Fe}_3\text{O}_4/\text{NF}$  sample merely requires an overpotential of 198 mV to achieve a current density of  $10 \text{ mA cm}^{-2}$ , much smaller than those of the benchmark  $\text{IrO}_2/\text{NF}$  (287 mV) catalyst and the recently reported catalysts (Fig. 3c and Table S3), indicating the introduction of Cr could further improve the OER activity of the heterostructure catalyst. In particular, the  $\text{Fe}(\text{Cr})\text{OOH}/\text{Fe}_3\text{O}_4/\text{NF}$  electrode exhibits an outstanding activity at high output as well. It requires only an overpotential of 241 mV to reach a current density of  $500 \text{ mA cm}^{-2}$ , which is lower than most reported OER catalysts in alkaline solution (Fig. 3d and Table S3). As shown in

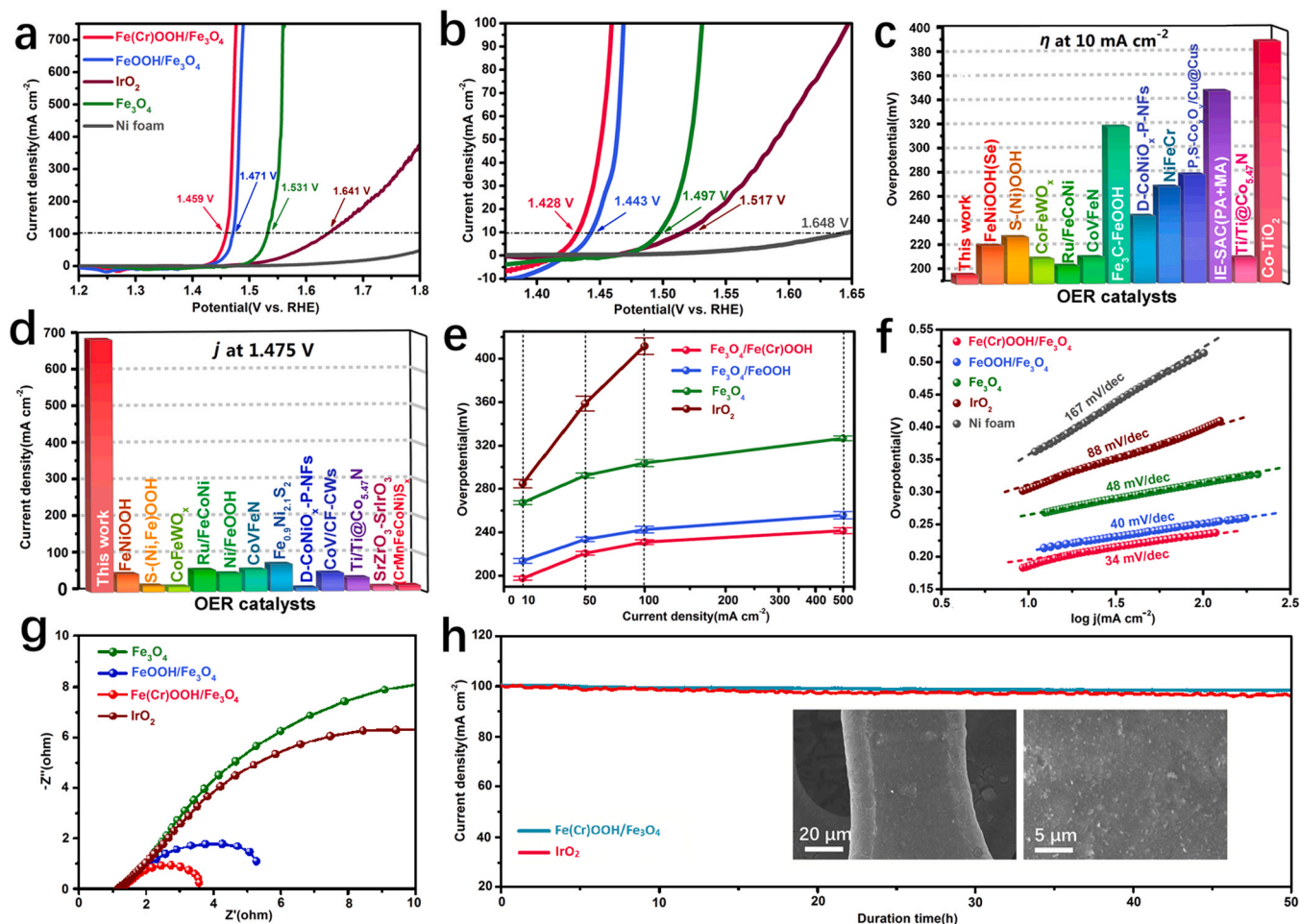


**Fig. 3.** LSV curves of different catalysts for OER at (a) high current densities and (b) low current densities in 1 M KOH. Comparison of (c) overpotentials and (d) current densities for OER among  $\text{Fe}(\text{Cr})\text{OOH}/\text{Fe}_3\text{O}_4$  with previously reported catalysts (Table S3). (e) Plots of  $j$  versus  $\eta$  with corresponding error bars. (f) Tafel plots and (g) Nyquist plots of different catalysts. (h) Chronoamperometry curves of  $\text{Fe}(\text{Cr})\text{OOH}/\text{Fe}_3\text{O}_4/\text{NF}$  and  $\text{IrO}_2/\text{NF}$ , inset, SEM images of  $\text{Fe}(\text{Cr})\text{OOH}/\text{Fe}_3\text{O}_4/\text{NF}$  after the OER test.

Fig. 3e, the parallel samples of Fe(Cr)OOH/Fe<sub>3</sub>O<sub>4</sub>/NF are also examined and the results show a stable performance with acceptable errors, proving the reliability and repeatability of the electrode. The Tafel slopes obtained for Fe(Cr)OOH/Fe<sub>3</sub>O<sub>4</sub>/NF, FeOOH/Fe<sub>3</sub>O<sub>4</sub>/NF, Fe<sub>3</sub>O<sub>4</sub>/NF, IrO<sub>2</sub>/NF and bare NF are 34, 40, 48, 88, and 167 mV dec<sup>-1</sup>, respectively. Obviously, the Fe(Cr)OOH/Fe<sub>3</sub>O<sub>4</sub>/NF has the smallest Tafel slope value, indicating the best reaction kinetics of Fe(Cr)OOH/Fe<sub>3</sub>O<sub>4</sub>/NF among these samples.

The electrochemical impedance spectroscopy (EIS) was performed to determine the electron transfer kinetics (Fig. 3g). The diameter of the semicircle is indexed to the charge transfer resistance ( $R_{ct}$ ) of the electrode. As expected, the Fe(Cr)OOH/Fe<sub>3</sub>O<sub>4</sub>/NF displays the smallest electron transfer resistance among the samples, indicating a high electronic conductivity of the electrode, and contributing to the highest OER performance especially at the large current densities. Furthermore, the double-layer capacitance ( $C_{dl}$ ) was measured to investigate the electrochemical surface area (ECSA) of the electrode, and the value was obtained from the linear relationship of the current densities at different scan rates (Fig. S5 and S6). The  $C_{dl}$  value of the Fe<sub>3</sub>O<sub>4</sub>/NF, Fe(Cr)OOH/Fe<sub>3</sub>O<sub>4</sub>/NF and IrO<sub>2</sub>/NF is 64, 9.97 and 4.3 mF cm<sup>-2</sup>, respectively. The OER current density normalized by ECSA is used to evaluate the intrinsic property of the as-prepared catalyst (Fig. S7). It is obvious that Fe(Cr)OOH/Fe<sub>3</sub>O<sub>4</sub>/NF presents a much more enhanced catalytic performance, indicating that the excellent OER performance of Fe(Cr)OOH/Fe<sub>3</sub>O<sub>4</sub>/NF mainly results from the intrinsically more active sites and good electrical conductivity [36,43,56].

The catalytic stability of the electrode is also an important factor for water electrolysis. The lifetime of the Fe(Cr)OOH/Fe<sub>3</sub>O<sub>4</sub>/NF and IrO<sub>2</sub>/NF was investigated by continuous electrolysis. As shown in Fig. 3h, the Fe(Cr)OOH/Fe<sub>3</sub>O<sub>4</sub>/NF electrode maintained a 100 mA cm<sup>-2</sup> anodic current density for 50 h, comparable to the stability of IrO<sub>2</sub>/NF. The good stability of the as-prepared catalyst can be attributed to two factors: Firstly, the as-prepared electrode is directly grown on the substrate and sintered at high temperature, which guarantees highly robust contact like a tree rooted in the ground, and thus contributes to good stability; Secondly, in the alkaline electrolyte, the dissolved metal cations will recombine with the OH<sup>-</sup> from the electrolyte and redeposit on the catalyst surface, thus causing almost no material loss [57]. The SEM images show that the morphology of Fe(Cr)OOH/Fe<sub>3</sub>O<sub>4</sub>/NF after the OER test remains unchanged (Fig. 3h inset), proving good mechanical stability of the electrode. EDX and XPS characterizations were also applied to check the post-OER catalysts, as presented in Fig. S8 and S9, no obvious change was observed in the content or chemical state, suggesting the good chemical stability of Fe(Cr)OOH/Fe<sub>3</sub>O<sub>4</sub> compound.

To reveal the effect of Cr content on the activity, Fe(Cr)OOH/Fe<sub>3</sub>O<sub>4</sub>/NF samples were prepared using impregnation solutions with various molar ratios ( $Cr^{3+}/[Fe^{3+} + Cr^{3+}] = 0.2, 0.4, 0.6, 0.8$ ). The SEM images in Fig. S10 and S11 show that Cr content has no impact on the morphology of the catalytic electrodes, and the XRD patterns of the different samples maintain the same as well (Fig. S12). The actual atom ratios of the catalyst presented in Fig. S13, Fig. S14 and S15 show that the optimum  $Cr^{3+}/(Fe^{3+} + Cr^{3+})$  ratio of the impregnation solution is 0.4. Fig. S16 shows that the Cr content has no obvious effect on the active surface area of the electrodes, while the sequence of charge-transfer resistance presents an order of  $(x = 0.4) < (x = 0.6) < (x = 0.2) < (x = 0.8) < (x = 0)$  ( $x = Cr^{3+}/(Fe^{3+} + Cr^{3+})$ , Fig. S17), which is consistent with the order of the OER activity (Fig. S15), indicating that the proper amount of Cr could improve the charge transfer and achieve the best OER performance. To further demonstrate the synergistic effect of the coupled heterostructure, FeOOH/NF and Fe(Cr)OOH/NF were also fabricated for comparison by directly using blank NF instead of Fe<sub>3</sub>O<sub>4</sub>/NF as the substrate via the same process. Fig. S18 shows the morphology of FeOOH/NF and Fe(Cr)OOH/NF, it could be found that a large number of agglomerated nanoparticles formed on the surface of NF, which is quite different from the uniform distribution of Fe(Cr)OOH/Fe<sub>3</sub>O<sub>4</sub>/NF. The LSV curves in Fig. S19 show that the activity

of Fe(Cr)OOH/NF is better than that of FeOOH/NF, but worse than that of Fe(Cr)OOH/Fe<sub>3</sub>O<sub>4</sub>/NF, confirming that the incorporation of Cr element and the coupling of FeOOH and Fe<sub>3</sub>O<sub>4</sub> could synergistically improve the OER activity of the catalyst.

### 3.3. Theoretical consideration

The theoretical model, as shown in Fig. 4a, was built to elucidate the synergistic effect between FeOOH and Fe<sub>3</sub>O<sub>4</sub> and the introduction of Cr in Fe(Cr)OOH/Fe<sub>3</sub>O<sub>4</sub> catalyst on the OER activity. The first-principle calculations were conducted via density functional theory (DFT) methods. Fig. 4b shows the calculated charge density of the model, demonstrating a charge redistribution at the interface between FeOOH and Fe<sub>3</sub>O<sub>4</sub>, and the electrons transfer from Cr to Fe, which is consistent with the XPS result. It is accepted that the OER process consists of four steps in an alkaline environment, and the reaction free energy ( $\Delta G$ ) of each step is calculated based on the optimized atomic structures with various adsorbed intermediates (Fig. S20, S21, and 4 c). The free energy diagrams show that, for all of these catalysts, the formation of O\* is the rate-determining step because of the highest  $\Delta G$  value. The theoretical overpotential ( $\eta$ ) of Fe<sub>3</sub>O<sub>4</sub> is calculated to be 1.62 V, while it reduced to 0.66 V for FeOOH/Fe<sub>3</sub>O<sub>4</sub>, indicating that the coupling of FeOOH and Fe<sub>3</sub>O<sub>4</sub> would decrease the energy barrier of OER. Though Cr site in Fe(Cr)OOH/Fe<sub>3</sub>O<sub>4</sub> shows a large  $\eta$  value of 1.32 V, the neighbouring Fe site presents the smallest  $\eta$  value of 0.55 V. This result indicates that Cr atom is relatively inert in OER, but it could efficiently enhance the catalytic activity of the neighbouring Fe atom. On the other point of view, of course, the high-content Cr would decrease the density of active sites (Fe) and thus degrade the catalytic performance, as confirmed in Fig. S14 and S15. To further reveal the contribution of Fe<sub>3</sub>O<sub>4</sub> to the activity, the model of pure FeOOH and Fe(Cr)OOH were also constructed and the optimized structures were presented in Fig. S22 and S23. The calculated results in Fig. S24 and S25 show that the  $\eta$  value of the Fe site in Fe(Cr)OOH is 0.81 V, which is lower than that of pristine FeOOH (1.32 V) but larger than that of Fe(Cr)OOH/Fe<sub>3</sub>O<sub>4</sub> (0.55 V), demonstrating the introduction of Cr and the coupling of FeOOH and Fe<sub>3</sub>O<sub>4</sub> could synergistically boost the OER activity. These calculation results are in good accordance with the experiments. Fig. 4e presents the electronic density of states (DOSs) of Fe<sub>3</sub>O<sub>4</sub>, FeOOH/Fe<sub>3</sub>O<sub>4</sub>, and Fe(Cr)OOH/Fe<sub>3</sub>O<sub>4</sub>. Unlike Fe<sub>3</sub>O<sub>4</sub> with a wide band-gap, FeOOH/Fe<sub>3</sub>O<sub>4</sub> presents new electronic states in the conduction band, indicating an enhanced electrical conductivity of the catalyst. Moreover, the incorporation of Cr further increases the DOS near the Fermi level of Fe(Cr)OOH/Fe<sub>3</sub>O<sub>4</sub> in comparison with that of FeOOH/Fe<sub>3</sub>O<sub>4</sub>, leading to higher conductivity. This computation result is consistent with the EIS analysis. Overall, the computations suggest that constructing the FeOOH/Fe<sub>3</sub>O<sub>4</sub> interface and introduction of Cr can optimize the intermediate binding and enhance the charge transfer capability, which is conducive for the OER process.

### 3.4. Exploration of practical applications

To ensure the feasibility of Fe(Cr)OOH/Fe<sub>3</sub>O<sub>4</sub>/NF electrode for practical industrial electrolysis, we then investigated the OER activity of the electrode in seawater (obtained from Bohai Sea) and sewage (taken from Xi'an sewer). To avoid the competition reactions [43] and enhance conductivity, KOH was added to the natural seawater and sewage. The concentration of KOH in the alkaline seawater and alkaline sewage is 1 M. The chemical oxygen-demanding substance (COD) value of the sewage was 322.5 mg L<sup>-1</sup>. And the electrolysis in the industrial alkaline electrolyte containing 5 M KOH was also performed. The CV curves of Fe(Cr)OOH/Fe<sub>3</sub>O<sub>4</sub>/NF in different electrolytes was shown in Fig. S26. Due to the difference in electrolyte composition, the potential of the Ni<sup>2+</sup>/Ni<sup>3+</sup> redox peak is slightly shifted. As presented in Fig. 5a–c, the Fe(Cr)OOH/Fe<sub>3</sub>O<sub>4</sub>/NF electrode shows outstanding OER activity in 5 M KOH aqueous electrolyte, which only requires small overpotentials of

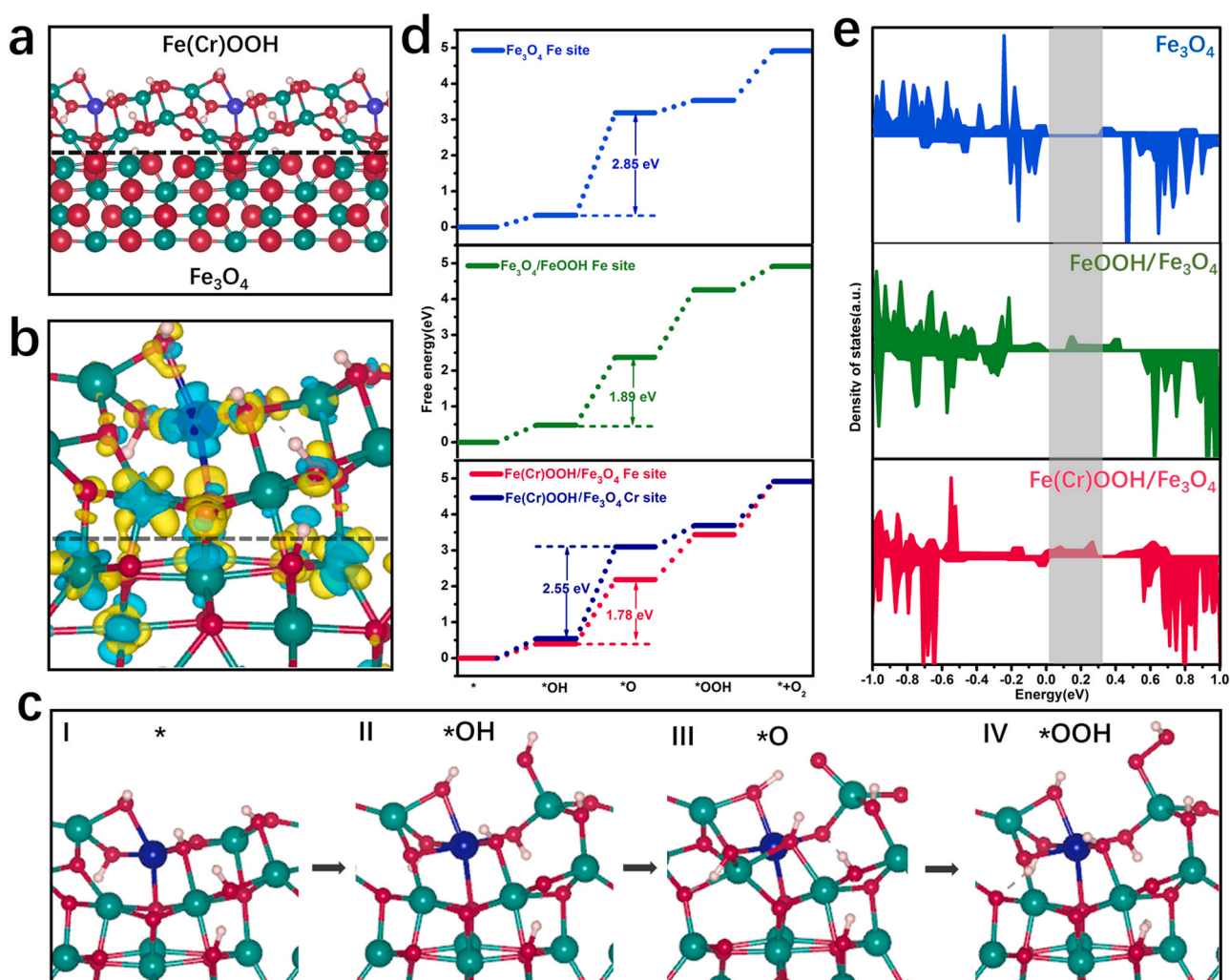


**Fig. 4.** Teal, maroon, indigo and white spheres represent the Fe, O, Cr, and H atoms, respectively. (a) The optimized structure of the Fe(Cr)OOH/Fe<sub>3</sub>O<sub>4</sub> model. (b) The differential charge density of Fe(Cr)OOH/Fe<sub>3</sub>O<sub>4</sub> (blue and yellow isosurfaces represent electron depletion and electron accumulation, respectively). (c) Schematic representation of the OER process on Fe(Cr)OOH/Fe<sub>3</sub>O<sub>4</sub>. (d) Free-energy profiles for OER on Fe<sub>3</sub>O<sub>4</sub>, FeOOH/Fe<sub>3</sub>O<sub>4</sub>, and Fe(Cr)OOH/Fe<sub>3</sub>O<sub>4</sub>. (e) Electronic density of states of Fe<sub>3</sub>O<sub>4</sub>, FeOOH/Fe<sub>3</sub>O<sub>4</sub>, and Fe(Cr)OOH/Fe<sub>3</sub>O<sub>4</sub>.

138, 171, and 201 mV to yield current densities of 10, 100, and 500 mA cm<sup>-2</sup>, respectively. Besides, the activity of the electrode declined slightly in alkaline wastewater and seawater. Despite this, the Fe(Cr)OOH/Fe<sub>3</sub>O<sub>4</sub> catalyst still reached current densities of 10 mA cm<sup>-2</sup> at overpotentials of 216 and 219 mV in alkaline sewage and seawater, respectively. Notably, the electrode preserves high performance at large current densities in both alkaline seawater (278 mV at 500 mA cm<sup>-2</sup>) and alkaline sewage (268 mV at 500 mA cm<sup>-2</sup>). In addition, oil contamination for the as-prepared catalysts were also tested. Hexane dyed with oil red was used as test oil. When the dyed oil was injected into water, it often floated on the water because of its lower density. When the oil drops contacted the surface during the rise, there was no oil residue on the surface of Fe(Cr)OOH/Fe<sub>3</sub>O<sub>4</sub>/NF. While for NF, a number of oil drops adhere to the surface (Fig. 5d). Combined with the results of contact angle measurements, Fe(Cr)OOH/Fe<sub>3</sub>O<sub>4</sub>/NF not only facilitates the contact of electrolyte, but also has anti-oil properties, thus leading to its excellent performance in sewage.

Furthermore, the stability of the catalyst under harsh conditions was also investigated. From Fig. 5j it can be observed that the current densities remain at around 100 mA cm<sup>-2</sup> for 100 h with a slight degradation in the three electrolytes, demonstrating an excellent OER durability of the catalyst. Moreover, the Fe(Cr)OOH/Fe<sub>3</sub>O<sub>4</sub>/NF shows a consistent performance after the sample being exposed to the air for six months

(Fig. 5i), demonstrating the excellent stability of the catalyst, which is quite important for the practical application. Compared with the complicated preparation process of other catalysts, the fabrication method of Fe(Cr)OOH/Fe<sub>3</sub>O<sub>4</sub>/NF is simple and well suited for large-scale production. Electrodes at scales from 25 to 400 cm<sup>2</sup> could be easily obtained by this strategy, as shown in Fig. 5e. The samples cut out from the area A, B, and C of 20 × 20 cm<sup>2</sup> Fe(Cr)OOH/Fe<sub>3</sub>O<sub>4</sub>/NF electrode (Fig. 5e) were characterized and measured to verify the reliability of the synthesis approach. The results indicate that the morphology and catalytic activity remain consistent across different parts of the sample (Fig. 5f–i and S27), indicating its great potential for mass production.

To go a step further toward industrial applications, a two-electrode electrolyzer was set up for water electrolysis (Fig. 6a), in which the OER catalyst of Fe(Cr)OOH/Fe<sub>3</sub>O<sub>4</sub> was paired with a robust HER catalyst of MoNi<sub>4</sub>/MoO<sub>2</sub> as previously reported by Feng et al. [58] (Fig. S28). The coupled Fe(Cr)OOH/Fe<sub>3</sub>O<sub>4</sub>(<sup>+</sup>)||MoNi<sub>4</sub>/MoO<sub>2</sub>(<sup>-</sup>) water electrolyzer was firstly investigated in 1 M KOH, and the electrolyzer could deliver a current density of 10 mA cm<sup>-2</sup> at a small cell voltage of 1.48 V, which is better than those of the state-of-the-art IrO<sub>2</sub>(<sup>+</sup>)||Pt/C(<sup>-</sup>) (1.63 V) and industrial used stainless steel(<sup>+</sup>)||Ni foam(<sup>-</sup>) (1.67 V), and superior to most of the recently reported water splitting electrocatalysts (Fig. 6c and Table S4). Interestingly, 1.48 V is exactly the value of the thermoneutral potential. Under adiabatic conditions, water electrolysis does not



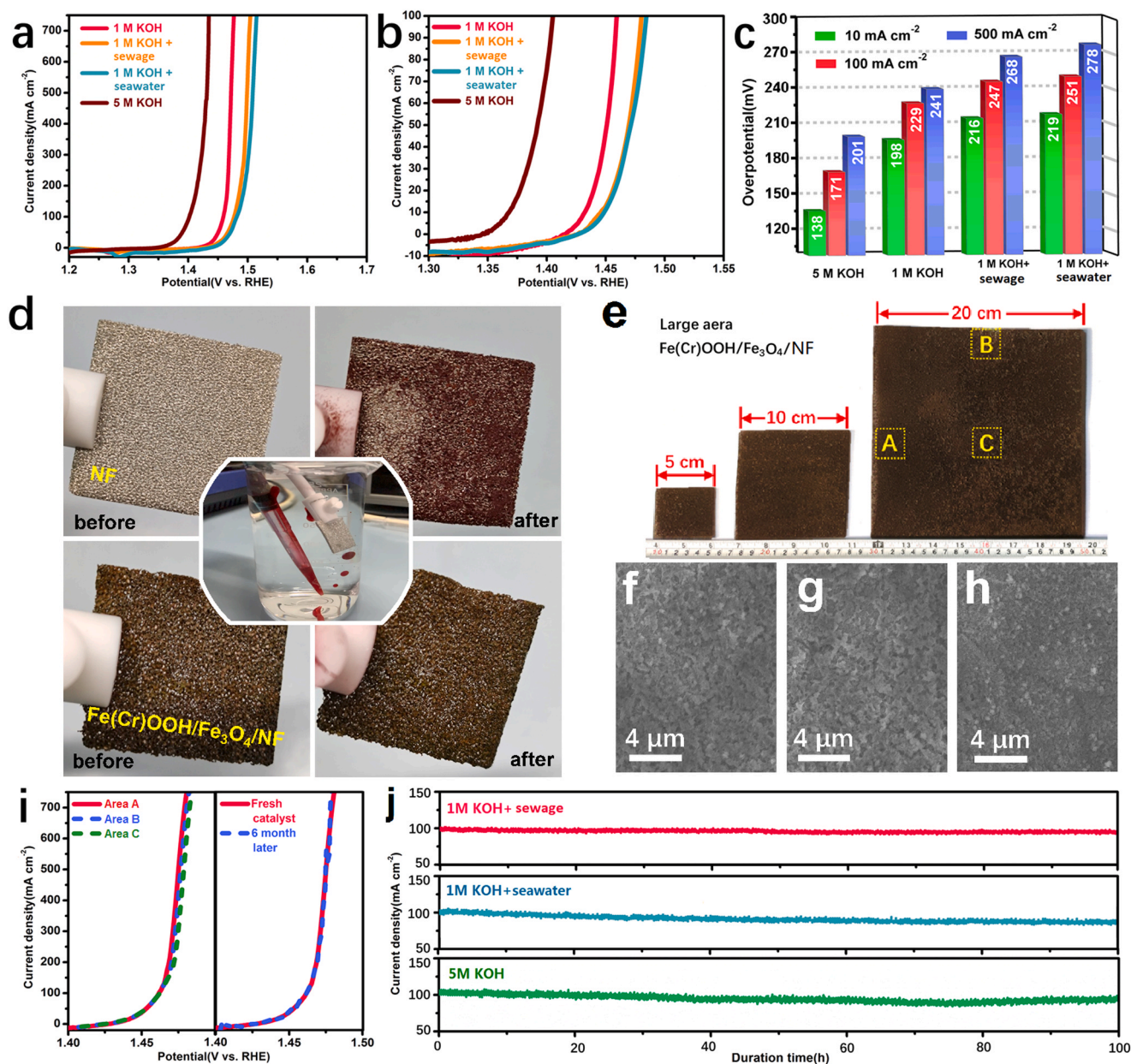


**Fig. 5.** Polarization curves for OER at (a) high current densities and (b) low current densities measured in different electrolytes. (c) Comparison of the overpotentials required to reach current densities of 10, 100, and 500 mA cm<sup>-2</sup> for the Fe(Cr)OOH/Fe<sub>3</sub>O<sub>4</sub>/NF. (d) Anti-oil properties of blank NF and Fe(Cr)OOH/Fe<sub>3</sub>O<sub>4</sub>/NF. (e) Photograph of Fe(Cr)OOH/Fe<sub>3</sub>O<sub>4</sub>/NF prepared at various scales, and corresponding SEM images of the selected areas, (f) area A, (g) area B and (h) area C. (i) The LSV curves of different Fe(Cr)OOH/Fe<sub>3</sub>O<sub>4</sub>/NF samples. (j) Lifetime tests for Fe(Cr)OOH/Fe<sub>3</sub>O<sub>4</sub>/NF in different electrolytes.

proceed when the cell voltage is lower than the thermoneutral potential. [59] Since the measurement environment is not adiabatic, the as-prepared Fe(Cr)OOH/Fe<sub>3</sub>O<sub>4</sub><sup>(+)</sup>||MoNi<sub>4</sub>/MoO<sub>2</sub><sup>(-)</sup> electrolyzer can sustain at a voltage below 1.48 V, which is attributed to energy exchange between the electrolyzer and the environment. Under this circumstance, the deficient energy is provided to the electrode by means of heat. The more detailed description is shown in Supporting Information. In particular, this electrolyzer shows excellent performance at large current densities, which could deliver high current densities of 100 and 500 mA cm<sup>-2</sup> at merely 1.55 and 1.66 V, respectively, superior to the IrO<sub>2</sub><sup>(+)</sup>||Pt/C<sup>(-)</sup> pair (1.86 V@100 mA cm<sup>-2</sup>, 2.16 V@500 mA cm<sup>-2</sup>) and stainless steel<sup>(+)</sup>||Ni foam<sup>(-)</sup> pair (1.89 V@100 mA cm<sup>-2</sup>, 2.01 V@500 mA cm<sup>-2</sup>), and exceeds the industrial standard (200–400 mA cm<sup>-2</sup> at 1.8–2.4 V) for water electrolysis. [17] The Fe(Cr)OOH/Fe<sub>3</sub>O<sub>4</sub><sup>(+)</sup>||MoNi<sub>4</sub>/MoO<sub>2</sub><sup>(-)</sup> electrolyzer could reach a large current

density of 450 mA cm<sup>-2</sup> at 1.65 V, which is superior to most of the recently reported catalysts (Fig. 6d and Table S4). Notably, the activity of stainless steel<sup>(+)</sup>||Ni foam<sup>(-)</sup> pair surpasses that of IrO<sub>2</sub><sup>(+)</sup>||Pt/C<sup>(-)</sup> as the current density exceeds 140 mA cm<sup>-2</sup>, indicating that the catalyst in powder form shows a lower activity at large current densities in contrast to that of the self-supported catalyst. Finally, the activity of the electrolyzer in near-industrial electrolytes was also investigated. As presented in Fig. 6e, the activity of electrolyzer in alkaline wastewater and seawater decreased slightly when compared to that in 1 M KOH, but still kept at a high level. The electrolyzer required a voltage of 1.49 V to reach a current density of 10 mA cm<sup>-2</sup> in both alkaline sewage and seawater, respectively (Fig. 6f). This performance is still superior to most recently reported catalysts in 1 M KOH (Fig. 6c and Table S4). The water electrolysis in alkaline wastewater can be powered by just a 1.5-volt battery (Fig. 6g and Video S1). A large amount of microbubbles

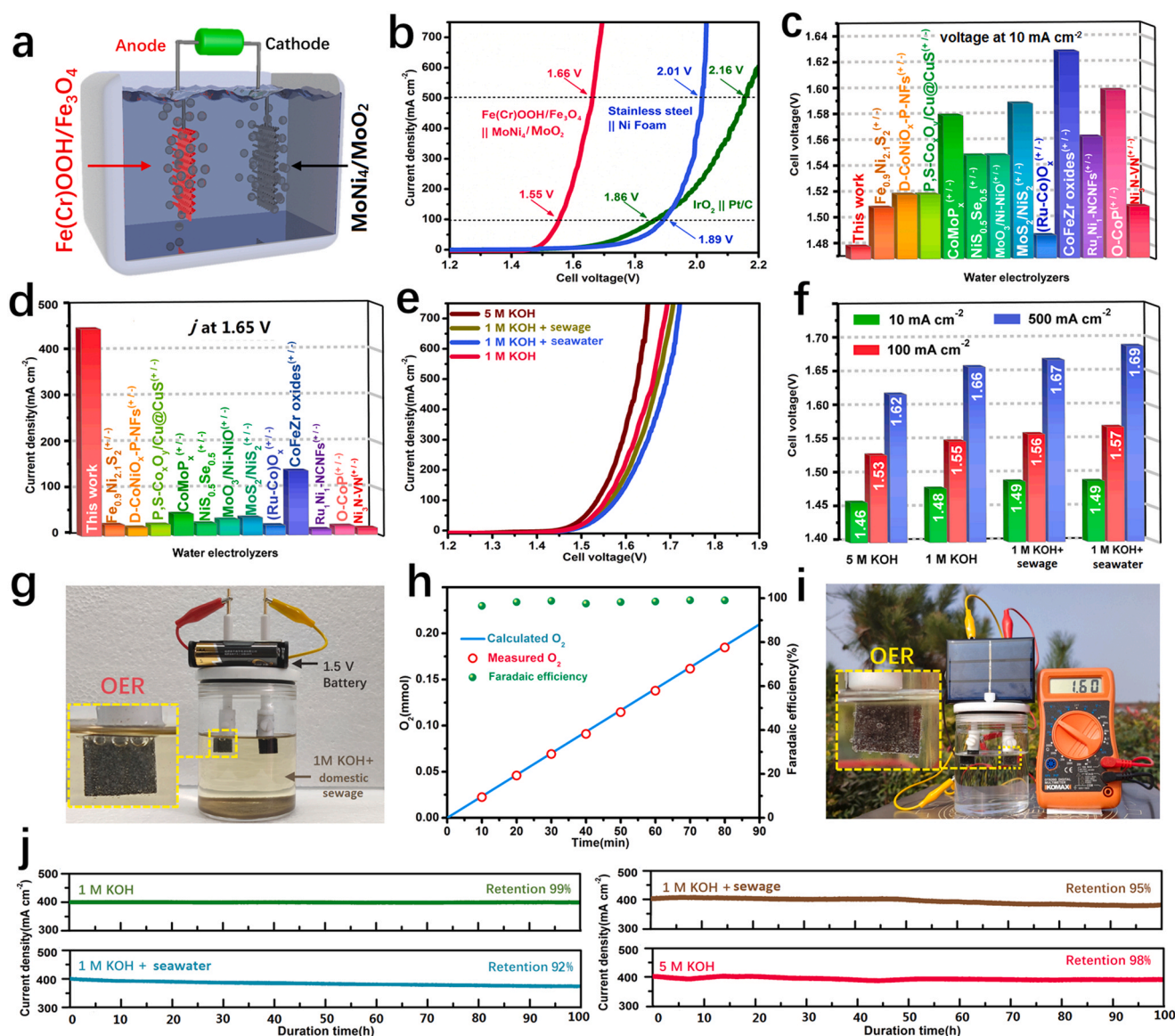


**Fig. 6.** (a) Schematic illustration of the  $\text{Fe(Cr)OOH/Fe}_3\text{O}_4^{(+)}||\text{MoNi}_4/\text{MoO}_2^{(-)}$  electrolyzer. (b) Polarization curves and comparison of (c) overpotentials and (d) current densities among  $\text{Fe(Cr)OOH/Fe}_3\text{O}_4^{(+)}||\text{MoNi}_4/\text{MoO}_2^{(-)}$  electrolyzer with previously reported catalysts (Table S4). (e) Polarization curves of the electrolyzer in different electrolytes and (f) comparison of the required voltages at current densities of 10, 100, and 500  $\text{mA cm}^{-2}$ . (g) Photo of the electrolyzer driven by a 1.5 V battery in alkaline sewage. (h) Faradaic efficiency of  $\text{Fe(Cr)OOH/Fe}_3\text{O}_4$  for OER. (i) Photo of the electrolyzer powered by a silicon solar cell in 1 M KOH. (j) Long-term stability tests conducted in different electrolytes.

emerges from the anode onset potential of the electrode. Impressively, the electrolyzer in 5 M KOH exhibits exceptional performance, which only requires a lower cell voltage of 1.46 V to generate a current density of 10  $\text{mA cm}^{-2}$  with a high voltage efficiency of 84.2%. The performance at high current densities is also remarkable, which deliver 100 and 500  $\text{mA cm}^{-2}$  at 1.53 and 1.62 V, respectively. The Faradaic efficiency of  $\text{Fe(Cr)OOH/Fe}_3\text{O}_4$  was investigated in 1 M KOH by a drainage method. As shown in Fig. 6h, the Faradaic efficiency is nearly 100%, indicates that there is no side reaction that occurs during the OER process. It is known that the most promising way to produce hydrogen is to combine water electrolysis with renewable energy. Thus we used a 1.6-volt solar cell to drive the  $\text{Fe(Cr)OOH/Fe}_3\text{O}_4^{(+)}||\text{MoNi}_4/\text{MoO}_2^{(-)}$  electrolyzer in 1 M KOH (Fig. 6 i). It could be observed that large amounts of bubbles generated from the surface of the electrode, proving its viability for operational water electrolysis systems. Furthermore, the  $\text{Fe(Cr)OOH/Fe}_3\text{O}_4^{(+)}||\text{MoNi}_4/\text{MoO}_2^{(-)}$  couple was measured in an anion exchange membrane water electrolyzer (AEMWE) with an electrode

area of  $1.5 \times 1.5 \text{ cm}^2$ , as shown in Fig. S30. The cathode and anode were separated by an anion exchange membrane, which can also separate the produced  $\text{H}_2$  and  $\text{O}_2$ . The volume ratio of the collected hydrogen to oxygen is 2:1. The electrolyzer could reach a current of 30 mA at a small cell voltage of 1.48 V in 1 M KOH (about 13  $\text{mA cm}^{-2}$ , quite similar with that measured through LSV), and the production rate of  $\text{H}_2$  is  $\sim 13.7 \text{ mL/h}$ . It is impressive that this electrolyzer shows outstanding durability at the high current density of 400  $\text{mA cm}^{-2}$  in different electrolytes as well (Fig. 6j). The  $\text{Fe(Cr)OOH/Fe}_3\text{O}_4^{(+)}||\text{MoNi}_4/\text{MoO}_2^{(-)}$  electrolyzer could maintain its performance without significant decay for 100 h when operated in 1 M and 5 M KOH solution. Meanwhile, it shows a minor current attenuation of 5% and 8% in alkaline sewage and seawater, respectively.

Supplementary material related to this article can be found online at [doi:10.1016/j.apcatb.2021.120847](https://doi.org/10.1016/j.apcatb.2021.120847).



## 4. Conclusion

In summary, this work proposes a facile and scalable approach to synthesize heterointerface between Fe(Cr)OOH and Fe<sub>3</sub>O<sub>4</sub> on Ni foam, by which the electrode with a large area of 400 cm<sup>2</sup> could be easily prepared. Benefiting from the good wettability, low charge transfer resistance and high intrinsic activity, the synthesized Fe(Cr)OOH/Fe<sub>3</sub>O<sub>4</sub>/NF electrode possesses an outstanding OER performance with small overpotentials of 198 and 241 mV required to reach current densities of 10 and 500 mA cm<sup>-2</sup>, respectively. DFT computations determined that the coupling of FeOOH and Fe<sub>3</sub>O<sub>4</sub> and the introduction of Cr could significantly enhance the conductivity and modulate the intermediate binding, resulting in a better electrical conductivity and lower energy barrier. The Fe(Cr)OOH/Fe<sub>3</sub>O<sub>4</sub>/NF electrode also presents excellent activity along with robust stability in 5 M KOH, alkaline seawater and domestic sewage. Overall, owing to the facile and easy scale-up synthesis method, as well as the excellent activity and stability of Fe(Cr)OOH/Fe<sub>3</sub>O<sub>4</sub>/NF, this work could provide references to the design of electrocatalyst for industrial large-scale water electrolysis.

## CRediT authorship contribution statement

**Lu Li:** Conceptualization, Formal analysis, Data curation, Investigation, Writing – original draft. **Gengwei Zhang:** Conceptualization, Formal analysis, Investigation, Data curation, Formal analysis, Writing – review & editing. **Bin Wang:** Supervision, Writing – review & editing. **Shengchun Yang:** Supervision, Conceptualization, Funding acquisition, Writing – review & editing.

## Declaration of Competing Interest

The authors declare that they have no known competing financial interests or personal relationships that could have appeared to influence the work reported in this paper.

## Acknowledgements

This work is supported by the Natural Science Foundation of Shaanxi Province (No. 2020JZ-02), National Natural Science Foundation of China (No. 51802255), the Joint Funds of the National Natural Science Foundation of China-State Grid Corporation (U1866203) and the Key Scientific and Technological Innovation Team of Shaanxi Province (2020TD-001). DFT calculations were supported by HPC Platform of Xi'an Jiaotong University. We thank Dr. Jiamei Liu from the Instrument Analysis Center of Xi'an Jiaotong University for the support in XPS characterizations. Dr. Xiaojing Zhang and Liqun Wang in School of Physics of Xi'an Jiaotong University are acknowledged for their kind help in TEM and SEM characterizations. We also thank Chuansheng Ma from Jia-Lab for Interface and Atomic Structure of Xi'an Jiaotong University for the support in TEM characterizations.

## Appendix A. Supporting information

Supplementary data associated with this article can be found in the online version at doi:10.1016/j.apcatb.2021.120847.

## References

- [1] C.G. Morales-Guio, L.A. Stern, X. Hu, Nanostructured hydrotreating catalysts for electrochemical hydrogen evolution, *Chem. Soc. Rev.* 43 (2014) 6555–6569, <https://doi.org/10.1039/c3cs60468c>.
- [2] F. Moureaux, P. Stevens, G. Toussaint, M. Chatenet, Timely-activated 316L stainless steel: a low cost, durable and active electrode for oxygen evolution reaction in concentrated alkaline environments, *Appl. Catal. B Environ.* 258 (2019), 117963, <https://doi.org/10.1016/j.apcatb.2019.117963>.
- [3] M.S. Balogun, W. Qiu, H. Yang, W. Fan, Y. Huang, P. Fang, G. Li, H. Ji, Y. Tong, A monolithic metal-free electrocatalyst for oxygen evolution reaction and overall

water splitting, *Energy Environ. Sci.* 9 (2016) 3411–3416, <https://doi.org/10.1039/c6ee01930g>.

- [4] M.S. Balogun, W. Qiu, Y. Huang, H. Yang, R. Xu, W. Zhao, G.R. Li, H. Ji, Y. Tong, Cost-effective alkaline water electrolysis based on nitrogen- and phosphorus-doped self-supportive electrocatalysts, *Adv. Mater.* 29 (2017) 1702095, <https://doi.org/10.1002/adma.201702095>.
- [5] F. Yang, T. Xiong, P. Huang, S. Zhou, Q. Tan, H. Yang, Y. Huang, M.S. Balogun, Nanostructured transition metal compounds coated 3D porous core-shell carbon fiber as monolith water splitting electrocatalysts: a general strategy, *Chem. Eng. J.* 423 (2021), 130279, <https://doi.org/10.1016/j.cej.2021.130279>.
- [6] Q. Tan, T. Xiong, F. Yang, P. Huang, D. Adekoya, Y. Huang, M.S. Balogun, Ni<sub>0.58</sub>Al<sub>0.42</sub> alloy growth on various conductive substrates and their use as advanced self-supportive electrocatalysts for boosted oxygen evolution catalysis, *J. Alloy. Compd.* 858 (2021), 157729, <https://doi.org/10.1016/j.jallcom.2020.157729>.
- [7] Y. Yang, L. Dang, M.J. Shearer, H. Sheng, W. Li, J. Chen, P. Xiao, Y. Zhang, R. J. Hamers, S. Jin, Highly active trimetallic NiFeCr layered double hydroxide electrocatalysts for oxygen evolution reaction, *Adv. Energy Mater.* 8 (2018) 1703189, <https://doi.org/10.1002/aenm.201703189>.
- [8] Z. Cai, X. Bu, P. Wang, J.C. Ho, J. Yang, X. Wang, Recent advances in layered double hydroxide electrocatalysts for the oxygen evolution reaction, *J. Mater. Chem. A* 7 (2019) 5069–5089, <https://doi.org/10.1039/c8ta11273h>.
- [9] X. Li, H. Wang, Z. Cui, Y. Li, S. Xin, J. Zhou, Y. Long, C. Jin, J.B. Goodenough, Exceptional oxygen evolution reactivities on CaCoO<sub>3</sub> and SrCoO<sub>3</sub>, *Sci. Adv.* 5 (2019) eaav6262, <https://doi.org/10.1126/sciadv.aav6262>.
- [10] J. Zhang, L. Yu, Y. Chen, X.F. Lu, S. Gao, X.W. Lou, Designed formation of double-shelled Ni-Fe layered-double-hydroxide nanocages for efficient oxygen evolution reaction, *Adv. Mater.* 32 (2020) 1906432, <https://doi.org/10.1002/adma.201906432>.
- [11] Z.P. Wu, X.F. Lu, S.Q. Zang, X.W. Lou, Non-noble-metal-based electrocatalysts toward the oxygen evolution reaction, *Adv. Funct. Mater.* 30 (2020) 1910274, <https://doi.org/10.1002/adfm.201910274>.
- [12] S.L. Zhang, B.Y. Guan, X.F. Lu, S. Xi, Y. Du, X.W. Lou, Metal atom-doped Co<sub>3</sub>O<sub>4</sub> hierarchical nanoplates for electrocatalytic oxygen evolution, *Adv. Mater.* 32 (2020) 2002235, <https://doi.org/10.1002/adma.202002235>.
- [13] Y. Huang, S.L. Zhang, X.F. Lu, Z.P. Wu, D. Luan, X.W. Lou, Trimetallic spinel NiCo<sub>2-x</sub>Fe<sub>x</sub>O<sub>4</sub> nanoboxes for highly efficient electrocatalytic oxygen evolution, *Angew. Chem. Int. Ed.* 60 (2021) 11841–11846, <https://doi.org/10.1002/anie.202103058>.
- [14] F.N.I. Sari, S. Abdillah, J.M. Ting, FeOOH-containing hydrated layered iron vanadate electrocatalyst for superior oxygen evolution reaction and efficient water splitting, *Chem. Eng. J.* 416 (2021), 129165, <https://doi.org/10.1016/j.cej.2021.129165>.
- [15] O. Kasian, S. Geiger, T. Li, J. Grote, K. Schweinar, S. Zhang, C. Scheu, D. Raabe, S. Cherevko, B. Gault, K.J.J. Mayrhofer, Degradation of iridium oxides via oxygen evolution from the lattice: correlating atomic scale structure with reaction mechanisms, *Energy Environ. Sci.* 12 (2019) 3548–3555, <https://doi.org/10.1039/C9EE01872G>.
- [16] S. Cherevko, S. Geiger, O. Kasian, N. Kulyk, J. Grote, A. Sava, B.R. Shrestha, S. Merzlikin, B. Breitbach, A. Ludwig, K.J.J. Mayrhofer, Oxygen and hydrogen evolution reactions on Ru, RuO<sub>2</sub>, Ir, and IrO<sub>2</sub> thin film electrodes in acidic and alkaline electrolytes: a comparative study on activity and stability, *Catal. Today* 262 (2016) 170–180, <https://doi.org/10.1016/j.cattod.2015.08.014>.
- [17] H. Zhou, F. Yu, Q. Zhu, J.S., F. Qin, L. Yu, J. Bao, Y. Yu, S. Chen, Z. Ren, Water splitting by electrolysis at high current densities under 1.6 volts, *Energy Environ. Sci.* 11 (2018) 2858–2864, <https://doi.org/10.1039/c8ee00927a>.
- [18] W. Jiang, T. Tang, Y. Zhang, J. Hu, Synergistic modulation of non-precious-metal electrocatalysts for advanced water splitting, *Acc. Chem. Res.* 53 (2020) 1111–1123, <https://doi.org/10.1021/acs.accounts.0c00127>.
- [19] M.F. Lagadec, A. Grimaud, Water electrolyzers with closed and open electrochemical systems, *Nat. Mater.* 19 (2020) 1140–1150, <https://doi.org/10.1038/s41563-020-0788-3>.
- [20] J. Song, C. Wei, Z. Huang, C. Liu, L. Zeng, X. Wang, Z.J. Xu, A review on fundamentals for designing oxygen evolution electrocatalysts, *Chem. Soc. Rev.* 49 (2020) 2196–2214, <https://doi.org/10.1039/c9cs00607a>.
- [21] Z.W. Seh, J. Kibsgaard, C.F. Dickens, I. Chorkendorff, J.K. Nørskov, T.F. Jaramillo, Combining theory and experiment in electrocatalysis: insights into materials design, *Science* 355 (2017) eaad4998, <https://doi.org/10.1126/science.aad4998>.
- [22] R. Gao, D. Yan, Recent development of Ni/Fe-Based micro/nanostructures toward photo/electrochemical water oxidation, *Adv. Energy Mater.* 10 (2019) 1900954, <https://doi.org/10.1002/aenm.201900954>.
- [23] S. Niu, W. Jiang, T. Tang, L. Yuan, H. Luo, J. Hu, Autogenous growth of hierarchical NiFe(OH)<sub>x</sub>/FeS nanosheet-on-microsheet arrays for synergistically enhanced high-output water oxidation, *Adv. Funct. Mater.* 29 (2019) 1902180, <https://doi.org/10.1002/adfm.201902180>.
- [24] C. Liang, P. Zou, A. Nairan, Y. Zhang, J. Liu, K. Liu, S. Hu, F. Kang, H. Fan, C. Yang, Exceptional performance of hierarchical Ni-Fe oxyhydroxide@NiFe alloy nanowire array electrocatalysts for large current density water splitting, *Energy Environ. Sci.* 13 (2020) 86–95, <https://doi.org/10.1039/c9ee02388g>.
- [25] L. Yu, L. Wu, B. McElhenny, S. Song, D. Luo, F. Zhang, Y. Yu, S. Chen, Z. Ren, Ultrafast room-temperature synthesis of porous S-doped Ni/Fe (oxy) hydroxide electrodes for oxygen evolution catalysis in seawater splitting, *Energy Environ. Sci.* 13 (2020) 3439–3446, <https://doi.org/10.1039/d0ee00921k>.
- [26] M. Gao, J. Zeng, Q. Zhang, C. Yang, X. Li, Y. Hua, C. Xu, Scalable one-step electrochemical deposition of nanoporous amorphous S-doped NiFe<sub>2</sub>O<sub>4</sub>/Ni<sub>3</sub> Fe composite films as highly efficient electrocatalysts for oxygen evolution with



- ultrahigh stability, *J. Mater. Chem. A* 6 (2018) 1551–1560, <https://doi.org/10.1039/c7ta08474a>.
- [27] N.K. Chaudhari, H. Jin, B. Kim, K. Lee, Nanostructured materials on 3D nickel foam as electrocatalysts for water splitting, *Nanoscale* 9 (2017) 12231–12247, <https://doi.org/10.1039/c7nr04187j>.
- [28] T. Kou, S. Wang, Y. Li, Perspective on high-rate alkaline water splitting, *ACS Mater. Lett.* 3 (2021) 224–234, <https://doi.org/10.1021/acsmaterialslett.0c00536>.
- [29] L. Yang, H. Liu, H. Shen, Y. Huang, S. Wang, L. Zheng, D. Cao, Physically adsorbed metal ions in porous supports as electrocatalysts for oxygen evolution reaction, *Adv. Funct. Mater.* 30 (2020) 1909889, <https://doi.org/10.1002/adfm.201909889>.
- [30] S. Niu, W. Jiang, Z. Wei, T. Tang, J. Ma, J. Hu, L. Wan, Se-doping activates FeOOH as cost-effective and efficient electrochemical water oxidation, *J. Am. Chem. Soc.* 141 (2019) 7005–7013, <https://doi.org/10.1021/jacs.9b01214>.
- [31] F. Li, J. Du, X. Li, J. Shen, Y. Wang, Y. Zhu, L. Sun, Integration of FeOOH and zeolitic imidazolate framework-derived nanoporous carbon as an efficient electrocatalyst for water oxidation, *Adv. Energy Mater.* 8 (2018) 1702598, <https://doi.org/10.1002/aenm.201702598>.
- [32] R. Subbaraman, D. Tripkovic, K. Chang, D. Strmcnik, A.P. Paulikas, P. Hirunsit, M. Chan, J. Greeley, V. Stamenkovic, N.M. Markovic, Trends in activity for the water electrolyser reactions on 3d M (Ni, Co, Fe, Mn) hydr(oxy)oxide catalysts, *Nat. Mater.* 11 (2012) 550–557, <https://doi.org/10.1038/nmat3313>.
- [33] T. Tang, W. Jiang, S. Niu, L. Yuan, J. Hu, L. Wan, Hetero-coupling of a carbonate hydroxide and sulfide for efficient and robust water oxidation, *J. Mater. Chem. A* 7 (2019) 21959–21965, <https://doi.org/10.1039/c9ta07882g>.
- [34] M. Zheng, K. Guo, W. Jiang, T. Tang, X. Wang, P. Zhou, J. Du, Y. Zhao, C. Xu, J. Hu, When MoS<sub>2</sub> meets FeOOH: a “one-stone-two-birds” heterostructure as a bifunctional electrocatalyst for efficient alkaline water splitting, *Appl. Catal. B Environ.* 244 (2019) 1004–1012, <https://doi.org/10.1016/j.apcatb.2018.12.019>.
- [35] Y. Luo, H. Yang, P. Ma, S. Luo, Z. Zhao, J. Ma, Fe<sub>3</sub>O<sub>4</sub>/CoO interfacial nanostructure supported on carbon nanotubes as a highly efficient electrocatalyst for oxygen evolution reaction, *ACS Sustain. Chem. Eng.* 8 (2020) 3336–3346, <https://doi.org/10.1021/acssuschemeng.9b07292>.
- [36] C. Qiu, S. He, Y. Wang, Q. Wang, C. Zhao, Interfacial engineering FeOOH/CoO nanoneedle array for efficient overall water splitting driven by solar energy, *Chem. Eur. J.* 26 (2020) 4120–4127, <https://doi.org/10.1002/chem.201904352>.
- [37] M. Cai, R. Pan, W. Liu, X. Luo, C. Chen, H. Zhang, M. Zhong, Laser-assisted doping and architecture engineering of Fe<sub>3</sub>O<sub>4</sub> nanoparticles for highly enhanced oxygen evolution reaction, *ChemSusChem* 12 (2019) 3562–3570, <https://doi.org/10.1002/cssc.201901020>.
- [38] X. Li, Z. Kou, S. Xi, W. Zang, T. Yang, L. Zhang, J. Wang, Porous NiCo<sub>2</sub>S<sub>4</sub>/FeOOH nanowire arrays with rich sulfide/hydroxide interfaces enable high OER activity, *Nano Energy* 78 (2020), 105230, <https://doi.org/10.1016/j.nanoen.2020.105230>.
- [39] W. Luc, Z. Jiang, J.G. Chen, F. Jiao, Role of surface oxophilicity in copper-catalyzed water dissociation, *ACS Catal.* 8 (2018) 9327–9333, <https://doi.org/10.1021/acscatal.8b01710>.
- [40] J. Kim, H. Jung, S. Jung, J. Hwang, D.Y. Kim, N. Lee, K. Kim, H. Kwon, Y. Kim, J. Han, J. Kim, Tailoring binding abilities by incorporating oxophilic transition metals on 3D nanostructured Ni arrays for accelerated alkaline hydrogen evolution reaction, *J. Am. Chem. Soc.* 143 (2021) 1399–1408, <https://doi.org/10.1021/jacs.0c10661>.
- [41] T. Liu, P. Diaio, Nickel foam supported Cr-doped NiCo<sub>2</sub>O<sub>4</sub>/FeOOH nanoneedle arrays as a high-performance bifunctional electrocatalyst for overall water splitting, *Nano Res.* 13 (2020) 3299–3309, <https://doi.org/10.1007/s12274-020-3006-3>.
- [42] W. Zang, T. Sun, T. Yang, S. Xi, M. Waqar, Z. Kou, Z. Lyu, Y. Feng, J. Wang, S. J. Pennycook, Efficient hydrogen evolution of oxidized Ni-N<sub>3</sub> defective sites for alkaline freshwater and seawater electrolysis, *Adv. Mater.* 33 (2021) 2003846, <https://doi.org/10.1002/adma.202003846>.
- [43] H. Song, H. Yoon, B. Ju, D. Lee, D. Kim, Electrocatalytic selective oxygen evolution of carbon-coated Na<sub>2</sub>Co<sub>1-x</sub>Fe<sub>x</sub>P<sub>2</sub>O<sub>7</sub> nanoparticles for alkaline seawater electrolysis, *ACS Catal.* 10 (2019) 702–709, <https://doi.org/10.1021/acscatal.9b04231>.
- [44] C. Xiang, K.M. Papadantonakis, N.S. Lewis, Principles and implementations of electrolysis systems for water splitting, *Mater. Horiz.* 3 (2016) 169–173, <https://doi.org/10.1039/c6mh00016a>.
- [45] M. Sanchez, E. Amores, D. Abad, L. Rodriguez, C. Clemente-Jul, Aspen Plus model of an alkaline electrolysis system for hydrogen production, *Int. J. Hydrog. Energy* 45 (2020) 3916–3929, <https://doi.org/10.1016/j.ijhydene.2019.12.027>.
- [46] Y. Duan, Z.Y. Yu, S.J. Hu, X.S. Zheng, C.T. Zhang, H.H. Ding, B.C. Hu, Q.Q. Fu, Z. L. Yu, X. Zheng, Scaled-up synthesis of amorphous NiFeMo oxides and their rapid surface reconstruction for superior oxygen evolution catalysis, *Angew. Chem. Int. Ed.* 58 (2019) 15772–15777, <https://doi.org/10.1002/anie.201909939>.
- [47] J. Rossmeisl, Z.-W. Qu, H. Zhu, G.-J. Kroes, J.K. Nørskov, Electrolysis of water on oxide surfaces, *J. Electroanal. Chem.* 607 (2007) 83–89, <https://doi.org/10.1016/j.jelechem.2006.11.008>.
- [48] Q. Ye, J. Li, X. Liu, X. Xu, F. Wang, B. Li, Surface pattern of NiCo hydroxide nanoplate arrays electrocatalysts for the oxygen evolution reaction, *J. Power Sources* 412 (2019) 10–17, <https://doi.org/10.1016/j.jpowsour.2018.10.075>.
- [49] Q. Kang, M. Li, Z. Wang, Q. Lu, F. Gao, Agaric-derived N-doped carbon nanorod arrays@ nanosheet networks coupled with molybdenum carbide nanoparticles as highly efficient pH-universal hydrogen evolution electrocatalysts, *Nanoscale* 12 (2020) 5159–5169, <https://doi.org/10.1039/c9nr10236a>.
- [50] W. Guo, D. Li, D. Zhong, S. Chen, G. Hao, G. Liu, J. Li, Q. Zhao, Loading FeOOH on Ni(OH)<sub>2</sub> hollow nanorods to obtain a three-dimensional sandwich catalyst with strong electron interactions for an efficient oxygen evolution reaction, *Nanoscale* 12 (2020) 983–990, <https://doi.org/10.1039/c9nr10236a>.
- [51] H. Zhang, Y. Zhao, Y. Zhang, M. Zhang, M. Cheng, J. Yu, H. Liu, M. Ji, C. Zhu, J. Xu, Fe<sub>3</sub>O<sub>4</sub> encapsulated in porous carbon nanobowls as efficient oxygen reduction reaction catalyst for Zn-air batteries, *Chem. Eng. J.* 375 (2019), 122058, <https://doi.org/10.1016/j.cej.2019.122058>.
- [52] Z. Luo, S. Martí-Sánchez, R. Nafria, G. Joshua, M. Mata, P. Guardia, C. Flox, C. Martínez-Boubeta, K. Simeonidis, J. Llorca, J.R. Morante, J. Arbiol, M. Ibáñez, A. Cabot, Fe<sub>3</sub>O<sub>4</sub>@NiFe<sub>x</sub>O<sub>y</sub> nanoparticles with enhanced electrocatalytic properties for oxygen evolution in carbonate electrolyte, *ACS Appl. Mater. Interfaces* 8 (2016) 29461–29469, <https://doi.org/10.1021/acsami.6b09888>.
- [53] Z. Wang, W. Liu, Y. Hu, M. Guan, L. Xu, H. Li, J. Bao, H. Li, Cr-doped CoFe layered double hydroxides: highly efficient and robust bifunctional electrocatalyst for the oxidation of water and urea, *Appl. Catal. B Environ.* 272 (2020), 118959, <https://doi.org/10.1016/j.apcatb.2020.118959>.
- [54] X. Liu, M. Gong, D. Xiao, S. Deng, J. Liang, T. Zhao, Y. Lu, T. Shen, J. Zhang, D. Wang, Turning waste into treasure: regulating the oxygen corrosion on Fe foam for efficient electrocatalysis, *Small* 16 (2020) 2000663, <https://doi.org/10.1002/smll.202000663>.
- [55] J. Guan, C. Li, J. Zhao, Y. Yang, W. Zhou, Y. Wang, G. Li, FeOOH-enhanced bifunctionality in Ni<sub>3</sub>N nanotube arrays for water splitting, *Appl. Catal. B Environ.* 269 (2020), 118600, <https://doi.org/10.1016/j.apcatb.2020.118600>.
- [56] X. Gao, X. Liu, W. Zang, H. Dong, Y. Pang, Z. Kou, P. Wang, Z. Pan, S. Wei, S. Mu, John Wang, Synergizing in-grown Ni<sub>3</sub>N/Ni heterostructured core and ultrathin Ni<sub>3</sub>N surface shell enables self-adaptive surface reconfiguration and efficient oxygen evolution reaction, *Nano Energy* 78 (2020), 105355, <https://doi.org/10.1016/j.nanoen.2020.105355>.
- [57] C.E. Beall, E. Fabbri, T.J. Schmidt, Perovskite oxide based electrodes for the oxygen reduction and evolution reactions: the underlying mechanism, *ACS Catal.* 11 (2021) 3094–3114, <https://doi.org/10.1021/acscatal.0c04473>.
- [58] J. Zhang, T. Wang, P. Liu, Z. Liao, S. Liu, X. Zhuang, M. Chen, E. Zschech, X. Feng, Efficient hydrogen production on MoNi<sub>4</sub> electrocatalysts with fast water dissociation kinetics, *Nat. Commun.* 8 (2017) 15437, <https://doi.org/10.1038/ncomms15437>.
- [59] K. Zeng, D. Zhang, Recent progress in alkaline water electrolysis for hydrogen production and applications, *Prog. Energy Combust. Sci.* 36 (2010) 307–326, <https://doi.org/10.1016/j.peccs.2009.11.002>.